WILEY | Hindawi

Research Article

Prediction of Equivalence Ratio in Combustion Flame Using Chemiluminescence Emission and Deep Neural Network

Sanghun Shin [ID],[1] **Minjun Kwon,**[1,2] **Sewon Kim,**[2] **and Hongyun So** [ID][1,3]

[1]*Department of Mechanical Engineering, Hanyang University, Seoul 04763, Republic of Korea*
[2]*Korea Institute of Industrial Technology (KITECH), Cheonan, Chungnam 31056, Republic of Korea*
[3]*Institute of Nano Science and Technology, Hanyang University, Seoul 04763, Republic of Korea*

Correspondence should be addressed to Hongyun So; hyso@hanyang.ac.kr

A reliable combustion monitoring system is essential to satisfy global carbon neutrality trends. As the concentrations of emissions and flame stability are associated with the air–fuel ratio, the equivalence ratio should be continuously evaluated. In this study, a deep neural network- (DNN-) based regression model is proposed to predict the equivalence ratio of turbulent diffusion flames. Chemiluminescence signals from the OH^*, CH^*, and C_2^* radicals were acquired as input features. In addition, three different optical sensing views were applied to consider the future general measurement conditions. Furthermore, a loss function comparison for model training and hyperparameter tuning techniques, such as random search and Bayesian optimization, were used to improve the prediction performance. Consequently, the enhanced DNN model showed reductions in the mean absolute error and root mean square error of ~17.84% and ~12.06%, respectively, compared with the initial model. In addition, a mean absolute percentage error and R-squared value of ~3.61% and ~0.9311, respectively, were obtained. Thus, a novel sensing method has been proposed for flame monitoring systems to realize future digital transformations in the combustion industry.

1. Introduction

Considering global environmental pollutants and human health concerns, the realization of a stable and efficient combustion system is imperative to satisfy emission regulations. Therefore, combustion pollutants, such as NO_x and CO, must be strictly controlled and monitored in industrial combustion applications [1–3]. Various studies have been conducted using different parameters, such as burner geometry [4, 5], ignition timing [6, 7], fuel type [8, 9], and equivalence ratio [9, 10], to enhance the combustion system efficiency. Among them, as combustion emissions are strongly affected by the equivalence ratio [10–12] which is related to the air–fuel ratio [13, 14], monitoring and controlling these parameters is important. Therefore, the equivalence ratio should be considered a crucial parameter to achieve flame stability and control the emission concentrations. The flow rates of air and fuel can be obtained directly using additional flow meters to calculate the equivalence ratio. However, direct sensing methods have some disadvantages, such as high cost and the need for regular offline calibration. Moreover, analytical instruments may be difficult to access physically because of complicated air/fuel supply systems in industrial applications. Therefore, facile soft-sensing methods that can measure the equivalence ratio of combustion systems during operation are required.

Over the past few decades, optical measurement methods, such as laser-induced breakdown spectroscopy (LIBS) [13, 15–17], tunable diode laser absorption spectroscopy (TDLAS) [18–21], intensified charge-coupled devices (ICCD) [4, 22, 23], spectrometry [24–26], and other methods [27–29] have been employed for flame monitoring. Specifically, as the indirect sensing methods can effectively characterize the combustion reaction through the flame, various studies have been conducted with different flame types and equivalence ratios recently, as shown in Table 1. For example, Wu et al. [17] applied LIBS to inverse diffusion methane-oxygen flame measurement to establish the

TABLE 1: Summary of recent studies for various flame monitoring techniques with different equivalence ratio.

Ref	Year	Flame	Fuel	Measurement technique	Equivalence ratio
[27]	2018	Premixed and diffusion flames	Propane	Ion current sensing	0.854–1.110
[32]	2019	Laminar and turbulent diffusion flames	Methane	UV imaging Line-scan hyperspectral imaging	0.7–1.2
[28]	2021	Lean premixed flames	Kerosene	Chemiluminescence by imaging spectrometer	0.53–0.80
[16]	2022	Turbulent partially premixed flames	NG, LPG	LIBS	0–1.4
[21]	2022	Turbulent flames	Kerosene	TDLAS	0.1–1.0
[17]	2022	Inverse diffusion flames	Methane	LIBS	0.30–0.70
[29]	2023	Premixed flames	Propane	Optical flame imaging	0.93–1.53

*NG: natural gas.

correlation between the overall equivalence ratio and LIBS emission spectra intensity. In addition, Liu et al. [21] used the TDLAS method for a scramjet model engine generating strong turbulent flow fields of the flame region with different equivalence ratios and flame temperatures. Furthermore, color and spatial characteristics were extracted using a high-speed camera by Yang et al. [29]. Through the radical chemiluminescence from optical flame imaging, the equivalence ratio measurement models between 0.93 and 1.53 were developed using a multiple linear regression.

As the chemiluminescence emissions from the OH^*, CH^*, and C_2^* radicals of flames are related to the equivalence ratio [24, 30], spectrometer data in the range of 200–700 nm can be utilized to predict the combustion conditions without additional equipment such as laser system and ICCD camera. However, for future real-time monitoring applications, scanning optical signals over the entire wavelength range is inefficient. Therefore, diverse studies have been conducted to obtain optical intensity values in specific wavelength regions (~309, ~431, and ~516 nm for OH^*, CH^*, and C_2^*, respectively) [22] demonstrating their considerable potential for effective flame diagnosis [22, 31, 32]. However, the optical signals can change depending on the position in the data acquisition process, yielding inaccurate results.

Artificial intelligence- (AI-) based models have been introduced in recent years to overcome conventional limitations in several fields. Specifically, AI models have been applied as computational algorithms to predict variables in complex situations where conventional physical sensors are unavailable or impractical, such as in autonomous vehicles [33, 34], manufacturing [35, 36], and environmental science [37, 38]. By utilizing deep learning techniques for data analysis and fusion from multiple sources, soft sensors can derive nonlinear relationships between physically coupled input and output data [39, 40]. Deep neural networks (DNN) were widely employed among the deep learning models for classification and regression problems [41–43]. The algorithm generally includes three types of layers of interconnected nodes: the input, output layer, and hidden layers. The number of nodes constituting the layer can be determined through appropriate hyperparameter tuning algorithms including grid search, random search, and Bayesian optimization [44, 45]. After the DNN model is established, it iteratively updates the training parameters through backpropagation considering loss function and error between actual and predicted values. In addition, as trained data-driven models can perform rapid calculations for output generation, these algorithms have considerable potential for real-time monitoring [46]. Furthermore, virtual sensors can be integrated into existing control systems, thereby enabling a more efficient and precise operation of industrial processes.

In this study, a DNN model was used to predict the equivalence ratio of a turbulent diffusion flame of liquefied petroleum gas (LPG) using the chemiluminescence characteristics of flame radicals. For the input data, three different chemiluminescence radical intensities—OH^*, CH^*, and C_2^*—were adopted. The datasets for the model training, validation, and test processes were established using experimental methods with different equivalence ratio values. Additionally, three different acquisition view directions were applied to the datasets to consider general observation conditions in real applications. Subsequently, various loss functions were used for the DNN model training, and hyperparameter tuning methods were conducted to enhance the prediction accuracy. Finally, the results were calculated and compared using regression metrics. Thus, a facile virtual sensing method is proposed to achieve real-time equivalence ratio monitoring systems via simple flame detection that is stable at optical sensing positions for future optimized combustion control and smart energy systems.

2. Experimental Setup for Combustion System

The experimental setup to implement combustion reactions and obtain datasets comprises three main components: a gas supply system for providing fuel and air, a combustion furnace for combustion reaction, and a spectrometer system used for optical measurements, as seen in Figure 1(a). Figure 1(b) shows the schematic of the combustion furnace used for the acquisition of chemiluminescence data. Other parameters influencing combustion characteristics, such as room temperature, pressure, humidity, and fuel speed, were assumed or set to constant values in all measurement cases to focus on the predictability of chemiluminescence signals as input data. Commercial gas (LPG) fuel and an air-staged diffusion flame burner with a maximum heat load of 40,000 kcal/h were used in the combustion system. For the gas burner, combustion air was supplied through a flame stabilizer. The LPG was initially mixed with air near the fuel
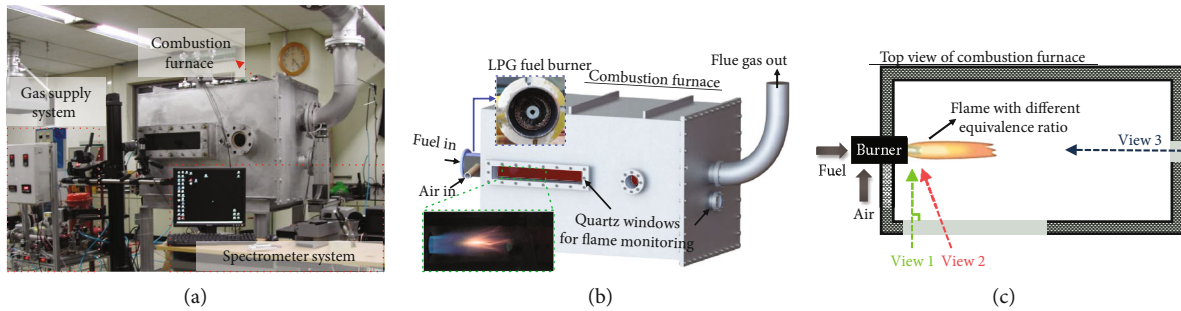
FIGURE 1: Schematic of the overall experimental setup for the dataset acquisition. (a) Photograph of measurement setup for dataset acquisition. (b) Experimental setup to generate turbulent diffusion flame. (c) Top view of the combustion furnace to obtain optical signals with different views.

nozzle at the center of the burner. In addition, air was supplied with tangential momentum from outside the burner. Furthermore, a perforated shape of the flame stabilizer was used for stable flame generation. A rectangular combustion furnace with the width, height, and length of 800, 800, and 1200 mm, respectively, was constructed for the test bed. In addition, rectangular and circular quartz windows were installed on the side and rear walls of the furnace to allow for optical flame measurements. The gas flow rate was measured using a rotameter at constant pressure and regulated using a pressure regulator. Prior to the supply of the gas to the burner, its pressure was reduced to 1000 mmAq using a regulator. Moreover, the supplied gas and air flow rate were controlled constantly using a needle valve and proportional-integral-derivative control, respectively.

As shown in Figure 1(c), three different views of flame detection, namely, vertical, diagonal, and horizontal views (hereafter referred to as view 1, view 2, and view 3, respectively), were applied through quartz windows for chemiluminescence measurements to consider different observation position deviations owing to limited optical access in future applications. In addition, all the optical sensing views were oriented in the initial local area (50 mm away from the burner outlet in the axial direction) of flame formation. Furthermore, an angle of 60° was formed from the burner flow direction for view 2. For view 3, measurements were conducted from the rear at an angle of ~10°, encompassing the downstream zone of the flame. Finally, the optical head applied in the experiments utilized a 1-inch diameter lens (LB4879, Thorlabs, Inc.) to transmit flame chemiluminescence through an optical fiber (RPU3-214-1.5-SSSS, Fiber optics) with a core size of 214 μm, spectral range of 190–1100 nm, and numerical aperture of 0.22. The optical fiber was positioned at the focal length of the lens to enable line-of-sight measurements. For the combustion conditions, nine different equivalence ratio values in the range of 0.56 to 1 (i.e., lean combustion conditions) were applied to generate the flame. The equivalence ratio (Φ) can be calculated by dividing the actual weight ratio of the fuel and oxidizer by the stoichiometric weight ratio.

Spectrometer (SpectraPro-500i, Acton) measurements were conducted within a range of 250 to 550 nm with a resolution of 0.3 nm for the equivalence ratio of 0.83 to compare the intensity distribution depending on the
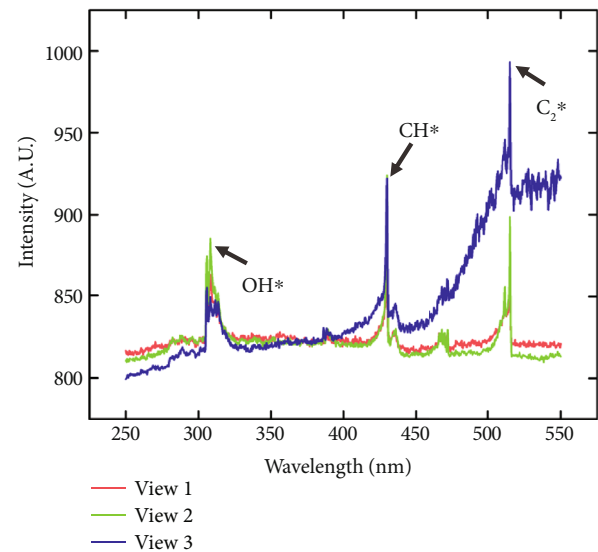

FIGURE 2: Intensity distribution of the generated flame depending on the wavelength with different measuring views.

wavelength with different view positions. As shown in Figure 2, three characteristic intensity peaks related to OH*, CH*, and C$_2$* were observed at the wavelengths of ~309, ~431, and ~516 nm, respectively. It should be noted that the three different radical regions with relatively high intensities compared to the other (refer to Figure 2) were selected for the data collection for the simple measurement, although the broadband CO$_2$* background emission can affect the other specific wavelength region [47]. However, despite the same combustion conditions, the results showed different intensity distributions in the wavelength range. Owing to the horizontal view (view 3), including the yellow and blue flame areas (see Figure 1), and the soot radiation effect [30, 48], an increasing trend was observed in the range of 400–550 nm. The background effect by the blackbody radiation can be subtracted by acquiring reference measurement without the target signal, as shown in previous studies [23, 49]. Additionally, normalization of baseline correction can be applied to further improve the quality of the spectral data. In subsequent experiments to acquire the datasets, selective detection was performed on the spectral regions of OH*, CH*, and C$_2$*, which represent the characteristics of the flame.
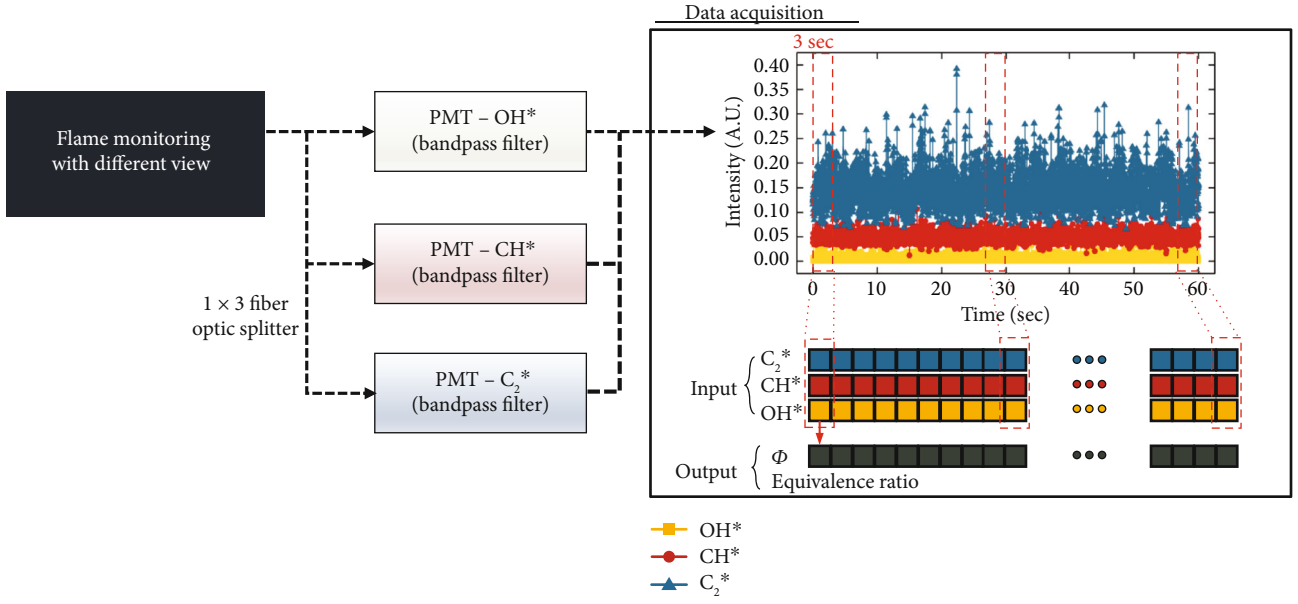
FIGURE 3: Workflow for data acquisition processes to establish the input/output dataset.
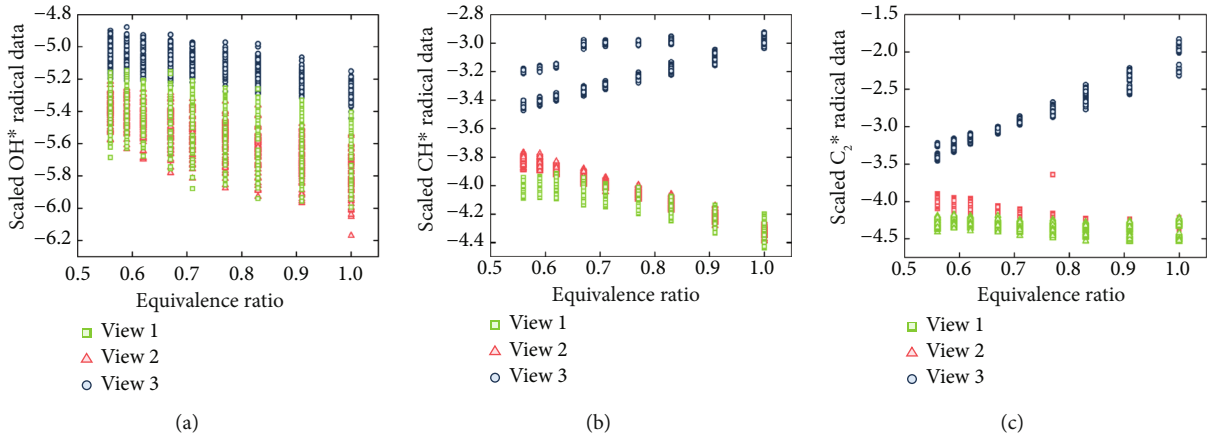

FIGURE 4: Obtained data distribution of the (a) OH*, (b) CH*, and (c) C_2* radicals.

3. Data Preparation for Model Training

Figure 3 shows the methodology and procedure for dataset acquisition using selective optical measurements. A 1×3 fiber optic splitter was utilized to transmit the same optical signal measured from the quartz window to three photomultiplier tubes (PMTs) (H5784-03, Hamamatsu). In addition, bandpass filters were applied to each PMT to capture specific radical chemiluminescence signals within a selective wavelength range. The center wavelength and peak transmission of the bandpass filters for OH*, CH*, and C_2* were 308.7, 432.2, and 511.3 nm, and 17.2%, 51.2%, and 66.2%, respectively. In this case, the measurement uncertainty, which can be calculated as the standard deviation, was obtained for the measured total equivalence ratios. Specifically, for OH*, the values were 0.005052, 0.004903, and 0.005405 for views 1, 2, and 3, respectively. Similarly, for CH*, the values were 0.006674, 0.006564, and 0.008646 for views 1, 2, and 3, respectively, and for C2*, the values were 0.006791,

0.006827, and 0.014247 for views 1, 2, and 3, respectively. It should be noted that the measurement uncertainty might be determined not only by the precision of the measurement devices but also by the fundamental characteristics of the turbulent flame. In the case of view 3, including the downstream zone of the flame, background radiation, and turbulent flame effect might affect the relatively high uncertainty values. Furthermore, the intensity data were averaged every 3 s, and their corresponding equivalence ratios were obtained for the input and output data. Subsequently, a natural logarithm was applied to the entire dataset to scale the data. Consequently, 2160 datasets were obtained and randomly split in a ratio of $7 : 1.5 : 1.5$ for the training, validation, and test datasets (i.e., 1512, 324, and 324, respectively) for training each prediction model.

Scaled OH*, CH*, and C_2* radical data were plotted as functions of the equivalence ratio, as depicted in Figures 4(a)–4(c), respectively, to analyze the measured dataset distribution. Owing to the short averaging time of
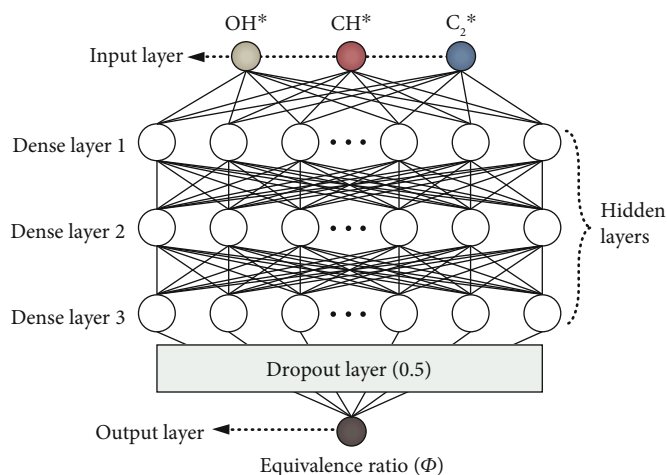
FIGURE 5: Illustration of the architecture of the DNN-based regression model.

3 s, and the turbulent flame, notably, some deviations were observed even in the same view and equivalence ratio conditions. As shown in Figure 4(a), as the equivalence ratio increased, the OH* radical data decreased under all viewing conditions. However, view 3 exhibited opposite trends to views 1 and 2 for the CH* and C$_2$* radical signals, as shown in Figures 4(b) and 4(c), respectively. These different tendencies may be attributed to the fact that the wavelength regions, including the chemiluminescence of CH* and C$_2$* radicals, could be influenced by the different view characteristics of view 3 compared with the other conditions, as demonstrated in Figure 2. Therefore, AI-based approaches can be used for precise measurements and real-time monitoring.

4. Deep Neural Network Regression Model

Figure 5 shows the DNN architecture for predicting the equivalence ratio using chemiluminescence signals. The DNN regression model consisted of input, output, hidden, and dropout layers. The input and output layers have three and one nodes for the radical signals and the corresponding equivalence ratio, respectively. For the input layer, the number of input features can be increased to apply other parameters such as intensity data of different wavelength regions to consider background radiations and combustion conditions for the enhanced prediction. In addition, three fully connected dense layers were used as hidden layers to extract the relationships between the features. Furthermore, a dropout layer with a dropout rate of 0.5 was added to prevent overfitting issues during the training processes [50]. With respect to the activation function, the rectified linear unit (ReLU) activation function was applied for the input and hidden layers, and the linear activation function was applied for the output layer for the nonlinearity of the DNN regression model. Therefore, the DNN model can effectively derive the nonlinear relationship between optical measurement results considering the uncertainty of turbulent flame and the equivalence ratio. Besides, by applying transfer learning techniques using pretrained DNNs, accurate models can be effectively developed with relatively small amount of data

for future applications with different combustion conditions (e.g., different flame, fuel, and burner types). The node numbers of the hidden layers (i.e., units 1, 2, and 3) and the learning rate were selected for the following hyperparameter tuning to search for the optimized hyperparameters for training the DNN regression model.

For data processing, algorithm realization, and training processes, Python-based frameworks were adopted using a cloud computing platform of Google Colaboratory Pro with Intel Xeon 2.20 GHz and Tesla P100 for the CPU and GPU, respectively. In addition, powerful open-source libraries, such as TensorFlow, Keras, and scikit-learn, were used. A min-max scaling preprocessing method was applied using the following equation to normalize the input log-scaled radical data and output equivalence ratio data:

$$X_{\text{scaled}} = \frac{X - X_{\min}}{X_{\max} - X_{\min}}, \qquad (1)$$

where X_{scaled}, $X_{\max}$, and $X_{\min}$ are the scaled, maximum, and minimum values of the data X, respectively. Therefore, the datasets were scaled from zero to one. Moreover, the Adam optimizer and 1000 epochs were used for model training. To evaluate the prediction performance of the trained regression models, several metrics, such as mean absolute error (MAE), root mean square error (RMSE), mean absolute percentage error (MAPE), and coefficient of determination (R-squared), were used, which can be calculated using the equations provided in Table 2. y_i, p_i, and $\bar{y}$ denote the actual value, predicted value, and the average of the actual value, respectively.

5. Results and Discussion

Various loss functions, such as the MAE, mean squared error (MSE), and Huber loss function, were applied for model training to compare the prediction performance of the regression model. The Huber loss function can be utilized to realize a robust regression model [51] by combining the advantages of both linear and squared losses with an

TABLE 2: Equations of regression metrics to evaluate the trained models.

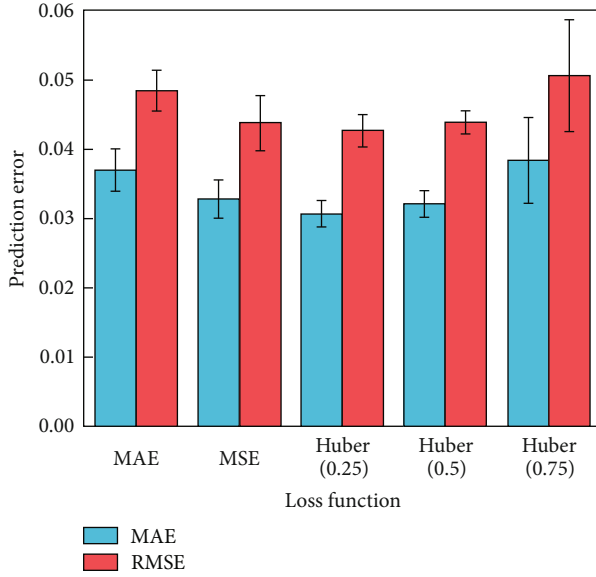| Metrics	MAE	RMSE	MAPE	R-squared
Equation	$\dfrac{1}{m}\sum_{i=1}^{m}\lvert y_i - p_i\rvert$	$\sqrt{\sum_{i=1}^{m}\dfrac{(y_i - p_i)^2}{m}}$	$\dfrac{1}{m}\sum_{i=1}^{m}\left\lvert\dfrac{y_i - p_i}{p_i}\right\rvert \times 100\%$	$1 - \dfrac{\sum_{i=1}^{m}(y_i - p_i)^2}{\sum_{i=1}^{m}(y_i - \bar{y})^2}$

FIGURE 6: Comparison of prediction error of the DNN regression model with different loss functions.

TABLE 3: Hyperparameter tuning results depending on the tuning techniques.

Tuning techniques	Selected hyperparameters	
	Unit 1	96
Random search	Unit 2	224
	Unit 3	128
	Learning rate	0.001
	Unit 1	256
Bayesian optimization	Unit 2	256
	Unit 3	160
	Learning rate	0.001

appropriate threshold that determines the transition between the losses, as shown in the following equations:

$$\text{Loss}_H(x) = \begin{cases} \dfrac{1}{2}x^2, & \text{if } \lvert x\rvert \le \alpha, \\[2mm] \alpha\left(\lvert x\rvert - \dfrac{1}{2}\alpha\right), & \text{if } \lvert x\rvert > \alpha, \end{cases} \tag{2}$$

where α is a positive real number and a threshold between the linear and quadratic returns of the prediction error of value x. Thereby, the Huber loss has the advantages of being robust to outliers and differentiable everywhere. However, α should be appropriately selected for the enhanced regression
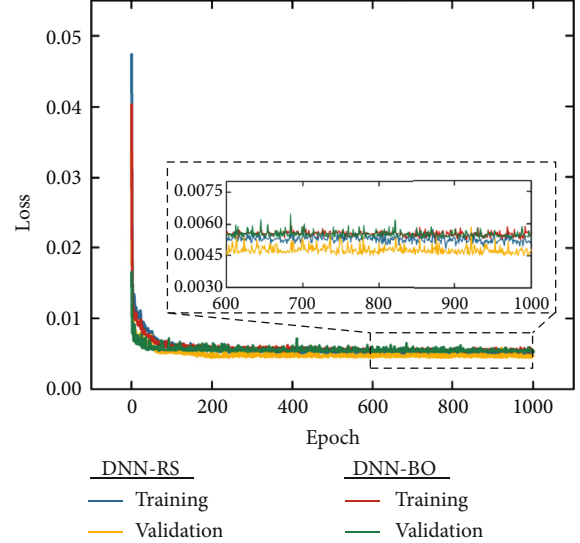

FIGURE 7: Training and validation loss trends of the DNN-based models depending on training epochs.

model. Parametric studies using α values of 0.25, 0.5, and 0.75 were conducted to determine the effective values. For the loss function comparison tests, units 1, 2, and 3 and the learning rate used were 32, 64, 128, and 0.01, respectively, for the DNN model (DNN-initial). Figure 6 shows the five average prediction results with different loss functions. The MAE and RMSE of the predicted and actual values were used to evaluate the prediction performances of the models. In comparison with the other cases, the model trained using the Huber loss function with $\alpha = 0.25$ demonstrated the smallest MAE and RMSE of 0.0307 and 0.0427, respectively. Thus, the Huber loss function with a threshold of 0.25 was selected for the subsequent model training and hyperparameter tuning processes.

As the internal hyperparameters of deep learning models are among the most critical factors that determine performance, optimized values need to be determined. In general, grid search [44, 52], random search [44, 53], and Bayesian optimization [54, 55] techniques are widely used to implement hyperparameter tuning processes. The grid search thoroughly explores hyperparameter combinations within a predefined set [44, 45]. Compared with a grid search, the random search technique randomly samples hyperparameters from a predefined distribution for a given number of iterations to determine satisfactory solutions [45, 56]. Bayesian optimization searches for optimized hyperparameter values based on Gaussian processes and acquisition functions [45, 55]. Therefore, while random search randomly selects and searches hyperparameters in the defined space, Bayesian optimization selects hyperparameters using
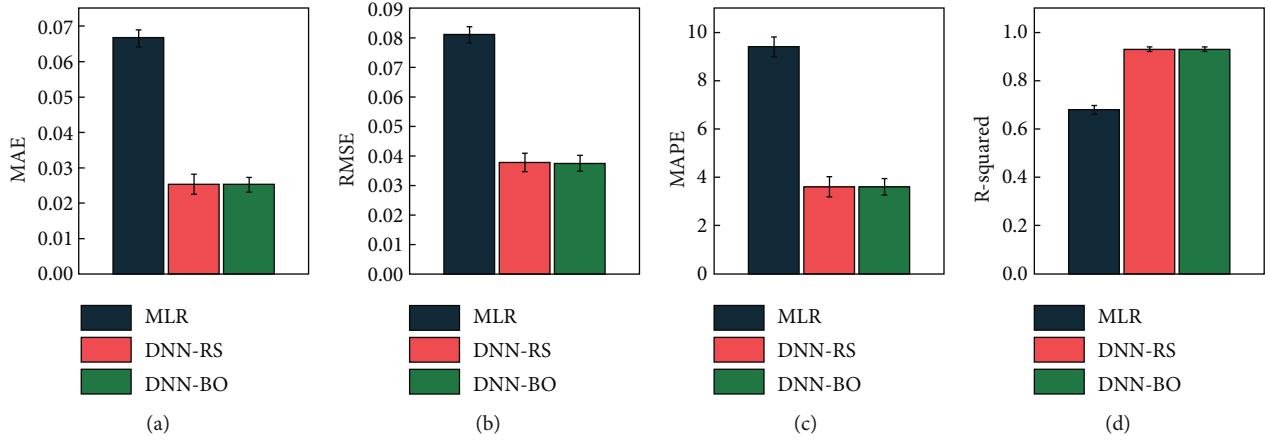
FIGURE 8: Prediction results of the three different regression models with evaluation metrics: (a) MAE, (b) RMSE, (c) MAPE, and (d) R-squared.
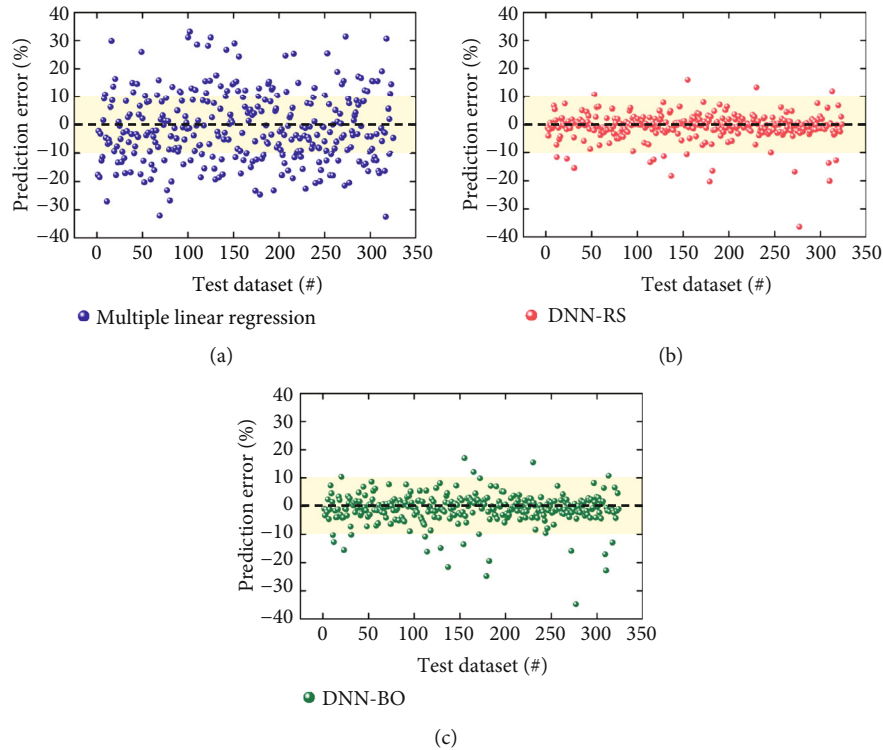

FIGURE 9: Distributions of predicted error for the test dataset of (a) MLR, (b) DNN-RS, and (c) DNN-BO models.

previous search results. In the present study, random search and Bayesian optimization techniques were employed to enhance the prediction performance of the DNN model. In the tuning process, a range of 32–256 for units 1, 2, and 3 of the hidden layers and a learning rate value among $1e$-2, $1e$-3, and $1e$-4 were selected to enhance the performance. Table 3 lists the best-searched hyperparameters for each tuner. Consequently, the random search technique selected 96, 224, 128, and $1e$-3, and the Bayesian optimization selected 256, 256, 160, and $1e$-3 for units 1, 2, 3, and the learning rate, respectively. Therefore, these parameters were applied to the established DNN algorithms (hereafter, DNN-RS and DNN-BO for tuned DNN algorithm using random search and Bayesian optimization, respectively), and their

prediction performances were compared using the training, validation, and test datasets.

Figure 7 shows the history of the training and validation losses of DNN-RS and DNN-BO during the model training processes. Overfitting did not occur, as demonstrated by the saturation tendencies of the losses. Subsequently, the training results were compared quantitatively and qualitatively using the test datasets. For comparison, an additional multilinear regression (MLR) model [57], a widely used conventional data-driven model, was fitted using the same datasets.

The average regression model prediction performances of MLR, DNN-RS, and DNN-BO were evaluated in terms of MAE, RMSE, MAPE, and R-squared values with 10 different newly shuffled datasets, as shown in Figure 8. The DNN-

based algorithms (i.e., DNN-RS and DNN-BO) exhibited similar prediction results, and their performances were improved compared with that of the previous DNN-initial architecture (before hyperparameter tuning). Specifically, the average MAE and RMSE of DNN-BO decreased by ~17.84% (~0.0307 to ~0.0252) and ~12.06% (~0.0427 to ~0.0376), respectively, compared with those of the previous DNN-initial architecture. Note that the DNN-BO model showed better prediction results than the MLR model. The MAE, RMSE, and MAPE values of DNN-BO were ~62.06%, ~53.69%, and ~61.65% smaller than those of the MLR, respectively. Furthermore, the MAPE values were approximately 3.62% and 3.61%, and the R-squared values were 0.9299 and 0.9311 for DNN-RS and DNN-BO, respectively, confirming a reliable prediction of the equivalence ratio.

The relative prediction errors were compared for 324 test data points to characterize the qualitative performance of the virtual sensing algorithms. Figures 9(a)–9(c) show examples of errors for MLR, DNN-RS, and DNN-BO, respectively, for the same test dataset. In this study, the prediction error of data number i between the ground truth (y_i) and prediction (p_i) values is defined as follows:

$$\text{Error}(\%) = 100 \times \frac{y_i - p_i}{y_i}. \tag{3}$$

As shown in Figure 9(a), compared with the DNN-based models, MLR predicted the equivalence ratio with a large error in the range of ±40%. By contrast, approximately 94% of the test datapoints were successfully predicted within ±10% error using the DNN-based models. In this case, although the chemiluminescence optical signals were obtained with different viewing directions, the equivalence ratio of the turbulent diffusion flame was predicted with only ~3.0% and ~3.5% errors with real data. Furthermore, it should be noted that only ~0.076 s was required to calculate the equivalence ratio for a single case on average, demonstrating the potential for real-time monitoring by utilizing the pretrained DNN model. More importantly, the prediction performance of data-driven models can be further enhanced using dataset augmentation and additional wavelengths of chemiluminescence signals. Moreover, the accuracy can be improved by acquiring a dataset utilizing a specific view direction if the measurement conditions are fixed in the actual environment. In conclusion, these results demonstrate the potential of the deep-learning-based regression model as a virtual sensing system for monitoring flame stability.

6. Conclusion

In this study, the equivalence ratio of a turbulent diffusion flame was predicted using experimental chemiluminescence data and deep-learning-based regression models. For the optical measurements, three different intensity signals from the OH^*, CH^*, and C_2^* radicals were obtained with various equivalence ratios in the range of 0.56–1. In addition, vertical, diagonal, and horizontal views were applied to consider general flame-monitoring environments. Subsequently, the prepared datasets were preprocessed for model training, validation, and testing. To derive the nonlinear relationships between the input and output, DNN-based deep learning regression models were trained and compared using various metrics, such as MAE, RMSE, MAPE, and R-squared. Subsequently, loss function comparison and hyperparameter tuning techniques, such as random search and Bayesian optimization, were applied to enhance the prediction performance. Consequently, DNN-BO showed ~17.84% and ~12.06% smaller MAE and RMSE values, respectively, than the initial DNN model. More importantly, the DNN-BO model showed an average MAPE and R-squared of only ~3.61% and ~0.9311, respectively. In addition, the prediction performances of the MLR- and DNN-based models were compared quantitatively and qualitatively. Note that the equivalence ratio could be successfully estimated using chemiluminescence data averaged for 3 s with the DNN models even if the measurement position changed. Furthermore, the trained DNN model needed only ~0.076 s on average to calculate the equivalence ratio, supporting the great potential for real-time monitoring applications. Thus, a simple, real-time, and novel virtual sensing technique has been proposed using a DNN-based regression model for future combustion monitoring and optimization.

Data Availability

The data that support the findings of this study are available from the corresponding author upon reasonable request.

Consent

All authors provided consent for publication.

Conflicts of Interest

There are no conflicts of interest to declare.

Authors' Contributions

Sanghun Shin and Minjun Kwon contributed equally to this work.

Acknowledgments

References

[1] C. Shan, W. Wang, C. Liu et al., "Regional CO emission estimated from ground-based remote sensing at Hefei site, China," *Atmospheric Research*, vol. 222, pp. 25–35, 2019.

[2] W. Yang, B. Wang, S. Lei et al., "Combustion optimization and NOx reduction of a 600 MWe down-fired boiler by rearrangement of swirl burner and introduction of separated over-fire air," *Journal of Cleaner Production*, vol. 210, pp. 1120–1130, 2019.

[3] F. Wang, S. Ma, H. Wang, Y. Li, Z. Qin, and J. Zhang, "A hybrid model integrating improved flower pollination algorithm-based feature selection and improved random forest for NO X emission estimation of coal-fired power plants," *Measurement*, vol. 125, pp. 303–312, 2018.

[4] H. Xu, F. Liu, S. Sun et al., "Influence of preheating and burner geometry on modeling the attachment of laminar coflow CH4/air diffusion flames," *Combustion and Flame*, vol. 191, pp. 381–393, 2018.

[5] Q. Yao, Y. Zhang, X. Wang, Z. Tian, G. Hu, and W. Du, "Investigation of NOx emission under different burner structures with the optimized combustion model," *Neurocomputing*, vol. 482, pp. 224–235, 2022.

[6] Y. Jin, H. Luo, G. Zhang et al., "Ignition timing effect on the combustion performance of hydrogen addition in methane fermentation gas in a local energy system," *Fuel*, vol. 324, article 124714, 2022.

[7] J. Gao, G. Tian, C. Ma, S. Xing, and L. Huang, "Three-dimensional numerical simulations on the effect of ignition timing on combustion characteristics, nitrogen oxides emissions, and energy loss of a hydrogen fuelled opposed rotary piston engine over wide open throttle conditions," *Fuel*, vol. 288, article 119722, 2021.

[8] G. M. Tashtoush, M. I. Al-Widyan, and A. M. Albatayneh, "Factorial analysis of diesel engine performance using different types of biofuels," *Journal of Environmental Management*, vol. 84, no. 4, pp. 401–411, 2007.

[9] A. A. Knizley, K. K. Srinivasan, S. R. Krishnan, and S. A. Ciatti, "Fuel and diluent effects on entropy generation in a constant internal energy–volume (uv) combustion process," *Energy*, vol. 43, no. 1, pp. 315–328, 2012.

[10] J. Zheng, J. Wang, Z. Zhao, D. Wang, and Z. Huang, "Effect of equivalence ratio on combustion and emissions of a dual-fuel natural gas engine ignited with diesel," *Applied Thermal Engineering*, vol. 146, pp. 738–751, 2019.

[11] J. M. Pires and E. C. Fernandes, "Combined effect of equivalence ratio and velocity gradients on flame stability and emission formation," *Fuel*, vol. 222, pp. 800–809, 2018.

[12] A. A. Al-Farayedhi, M. A. Antar, and A. Khan, "Effect of the equivalence ratio on the concentration of CH4/NO2/O2 combustion products," *International Journal of Energy Research*, vol. 23, no. 13, 1999.

[13] L. Merotto, M. Sirignano, M. Commodo, A. D'Anna, R. Dondè, and S. De Iuliis, "Experimental characterization and modeling for equivalence ratio sensing in non-premixed flames using chemiluminescence and laser-induced breakdown spectroscopy techniques," *Energy & Fuels*, vol. 31, no. 3, pp. 3227–3233, 2017.

[14] B. Ling, Z. Ling, M. Kuang et al., "Fuel-lean VOCs combustion in a porous burner stacked with alumina balls: a case for ethylene combustion," *International Journal of Energy Research*, vol. 43, no. 2, 2019.

[15] T. Badawy, M. Hamza, M. S. Mansour et al., "Lean partially premixed turbulent flame equivalence ratio measurements using laser-induced breakdown spectroscopy," *Fuel*, vol. 237, pp. 320–334, 2019.

[16] T. Badawy, M. Hamza, M. S. Mansour et al., "Flame stability and equivalence ratio assessment of turbulent partially premixed flames," *Fuel*, vol. 326, article 125107, 2022.

[17] R. Wu, J. Wei, B. Zhang et al., "In situ diagnostic investigation on the structure distribution of inverse diffusion flames based on laser-induced breakdown spectroscopy," *Fuel*, vol. 311, article 122540, 2022.

[18] C. Liu, Z. Cao, Y. Lin, L. Xu, and H. McCann, "Online cross-sectional monitoring of a swirling flame using TDLAS tomography," *IEEE Transactions on Instrumentation and Measurement*, vol. 67, no. 6, pp. 1338–1348, 2018.

[19] A. Huang, Z. Cao, W. Zhao, H. Zhang, and L. Xu, "Frequency-division multiplexing and main peak scanning WMS method for TDLAS tomography in flame monitoring," *IEEE Transactions on Instrumentation and Measurement*, vol. 69, no. 11, pp. 9087–9096, 2020.

[20] C. Liu, Z. Cao, F. Li, Y. Lin, and L. Xu, "Flame monitoring of a model swirl injector using 1D tunable diode laser absorption spectroscopy tomography," *Measurement Science and Technology*, vol. 28, no. 5, article 054002, 2017.

[21] X. Liu and Y. Ma, "Tunable diode laser absorption spectroscopy based temperature measurement with a single diode laser near 1.4 μm," *Sensors*, vol. 22, no. 16, p. 6095, 2022.

[22] Y. K. Jeong, C. H. Jeon, and Y. J. Chang, "Evaluation of the equivalence ratio of the reacting mixture using intensity ratio of chemiluminescence in laminar partially premixed CH4-air flames," *Experimental Thermal and Fluid Science*, vol. 30, no. 7, pp. 663–673, 2006.

[23] Y. Liu, J. Tan, M. Wan, L. Zhang, and X. Yao, "Quantitative measurement of OH* and CH* chemiluminescence in jet diffusion flames," *ACS Omega*, vol. 5, no. 26, pp. 15922–15930, 2020.

[24] T. García-Armingol, J. Ballester, and A. Smolarz, "Chemiluminescence-based sensing of flame stoichiometry: influence of the measurement method," *Measurement*, vol. 46, no. 9, pp. 3084–3097, 2013.

[25] J. Ballester, R. Hernández, A. Sanz, A. Smolarz, J. Barroso, and A. Pina, "Chemiluminescence monitoring in premixed flames of natural gas and its blends with hydrogen," *Proceedings of the Combustion Institute*, vol. 32, no. 2, pp. 2983–2991, 2009.

[26] C. Romero, X. Li, S. Keyvan, and R. Rossow, "Spectrometer-based combustion monitoring for flame stoichiometry and temperature control," *Applied Thermal Engineering*, vol. 25, no. 5-6, pp. 659–676, 2005.

[27] F. Li, Z. Cao, L. Xu, and Y. Xie, "Prediction of equivalence ratio in pulse combustor from ion current amplitude spectrum," *Fuel*, vol. 218, pp. 179–187, 2018.

[28] M. Vogel, M. Bachfischer, J. Kaufmann, and T. Sattelmayer, "Experimental investigation of equivalence ratio fluctuations in a lean premixed kerosene combustor," *Experiments in Fluids*, vol. 62, no. 5, p. 93, 2021.

[29] H. Yang, Y. Lai, X. Liu, H. Jiang, and J. Yang, "Equivalence ratio modelling of premixed propane flame by multiple linear regression using flame color and spatial characteristics," *Measurement Science Review*, vol. 23, no. 1, pp. 40–46, 2023.

[30] S. Kim, C. Lee, and M. Kwon, "Measurement of equivalence ratio using optical flame chemiluminescence sensor of turbulent diffusion flame," *International Journal of Electrical Energy*, vol. 3, no. 3, pp. 203–208, 2015.

[31] B. Higgins, M. Q. McQuay, F. Lacas, J. C. Rolon, N. Darabiha, and S. Candel, "Systematic measurements of OH chemiluminescence for fuel-lean, high-pressure, premixed, laminar flames," *Fuel*, vol. 80, no. 1, pp. 67–74, 2001.

[32] H. Zhu, C. Hu, Q. Guo, Y. Gong, and G. Yu, "Investigation on chemiluminescence and structure characteristics in CH4/O2 diffusion flames," *Experimental Thermal and Fluid Science*, vol. 102, pp. 595–602, 2019.

[33] R. Izquierdo, Á. Quintanar, D. F. Llorca et al., "Vehicle trajectory prediction on highways using bird eye view representations and deep learning," *Applied Intelligence*, vol. 53, no. 7, pp. 8370–8388, 2023.

[34] T. Fernando, S. Denman, S. Sridharan, and C. Fookes, "Deep inverse reinforcement learning for behavior prediction in autonomous driving: accurate forecasts of vehicle motion," *IEEE Signal Processing Magazine*, vol. 38, no. 1, pp. 87–96, 2021.

[35] J. Qin, F. Hu, Y. Liu et al., "Research and application of machine learning for additive manufacturing," *Additive Manufacturing*, vol. 52, article 102691, 2022.

[36] H. Yang, W. Wang, C. Li et al., "Deep learning-based X-ray computed tomography image reconstruction and prediction of compression behavior of 3D printed lattice structures," *Additive Manufacturing*, vol. 54, article 102774, 2022.

[37] B. Yang, Z. Xiao, Q. Meng et al., "Deep learning-based prediction of effluent quality of a constructed wetland," *Environ Sci Ecotechnology*, vol. 13, article 100207, 2023.

[38] B. Zhang, G. Zou, D. Qin, Y. Lu, Y. Jin, and H. Wang, "A novel encoder-decoder model based on read-first LSTM for air pollutant prediction," *Science of The Total Environment*, vol. 765, article 144507, 2021.

[39] Z. Han, Rahul, and S. de, "A deep learning-based hybrid approach for the solution of multiphysics problems in electrosurgery," *Computer Methods in Applied Mechanics and Engineering*, vol. 357, article 112603, 2019.

[40] Z. Tang, H. Dong, C. Zhang, S. Cao, and T. Ouyang, "Deep learning models for SO2 distribution in a 30 MW boiler via computational fluid dynamics simulation data," *ACS Omega*, vol. 7, no. 46, pp. 41943–41955, 2022.

[41] I. B. Basyigit, A. Genc, H. Dogan, F. A. Senel, and S. Helhel, "Deep learning for both broadband prediction of the radiated emission from heatsinks and heatsink optimization," *Engineering Science and Technology, an International Journal*, vol. 24, no. 3, pp. 706–714, 2021.

[42] J. Ni, D. Xiang, Z. Lin, C. Lopez-Martinez, W. Hu, and F. Zhang, "DNN-based PolSAR image classification on noisy labels," *IEEE Journal of Selected Topics in Applied Earth Observations and Remote Sensing*, vol. 15, pp. 3697–3713, 2022.

[43] S. Metlek, K. Kayaalp, I. B. Basyigit, A. Genc, and H. Dogan, "The dielectric properties prediction of the vegetation depending on the moisture content using the deep neural network model," *International Journal of RF and Microwave Computer-Aided Engineering*, vol. 31, no. 1, 2021.

[44] R. Taherdangkoo, Q. Liu, Y. Xing et al., "Predicting methane solubility in water and seawater by machine learning algorithms: application to methane transport modeling," *Journal of Contaminant Hydrology*, vol. 242, article 103844, 2021.

[45] A. Stuke, P. Rinke, and M. Todorović, "Efficient hyperparameter tuning for kernel ridge regression with Bayesian optimization," *Machine Learning: Science and Technology*, vol. 2, no. 3, article 035022, 2021.

[46] S. Shin, K. Baek, and H. So, "Rapid monitoring of indoor air quality for efficient HVAC systems using fully convolutional network deep learning model," *Building and Environment*, vol. 234, article 110191, 2023.

[47] T. F. Guiberti, D. Durox, and T. Schuller, "Flame chemiluminescence from CO2- and N2-diluted laminar CH4/air premixed flames," *Combustion and Flame*, vol. 181, pp. 110–122, 2017.

[48] R. Wu, F. Xie, J. Wei et al., "Study on soot emission characteristics of methane/oxygen inverse diffusion flame," *ACS Omega*, vol. 6, no. 36, pp. 23191–23202, 2021.

[49] S. Karnani and D. Dunn-Rankin, "Visualizing CH * chemiluminescence in sooting flames," *Combustion and Flame*, vol. 160, no. 10, pp. 2275–2278, 2013.

[50] N. Srivastava, G. Hinton, A. Krizhevsky, I. Sutskever, and R. Salakhutdinov, "Dropout: a simple way to prevent neural networks from overfitting," *Journal of Machine Learning Research*, vol. 15, pp. 1929–1958, 2014.

[51] M. Jia and C. Leng, "Multi-well dynamic liquid-level prediction method of pumping well based on dynamic and static information feature fusion neural network," *Transactions of the Institute of Measurement and Control*, vol. 45, no. 6, pp. 1099–1110, 2023.

[52] H. Bao, S. Wu, Z. Wu, G. Kang, X. Peng, and P. J. Withers, "A machine-learning fatigue life prediction approach of additively manufactured metals," *Engineering Fracture Mechanics*, vol. 242, article 107508, 2021.

[53] S. Shin, B. Ko, and H. So, "Noncontact thermal mapping method based on local temperature data using deep neural network regression," *International Journal of Heat and Mass Transfer*, vol. 183, article 122236, 2022.

[54] K. Tian, Z. Li, J. Zhang, L. Huang, and B. Wang, "Transfer learning based variable-fidelity surrogate model for shell buckling prediction," *Composite Structures*, vol. 273, article 114285, 2021.

[55] D. Kong, S. Wang, and P. Ping, "State-of-health estimation and remaining useful life for lithium-ion battery based on deep learning with Bayesian hyperparameter optimization," *International Journal of Energy Research*, vol. 46, no. 5, 2022.

[56] J. Bergstra and Y. Bengio, "Random search for hyperparameter optimization," *Journal of Machine Learning Research*, vol. 13, pp. 281–305, 2012.

[57] C. Wang, J. Yuan, J. Zhang, N. Deng, Z. Zhou, and F. Gao, "Multi-criteria comprehensive study on predictive algorithm of heating energy consumption of district heating station based on timeseries processing," *Energy*, vol. 202, article 117714, 2020.